Available online at www.sciencedirect.com

ScienceDirect

Geochimica et Cosmochimica Acta 250 (2019) 117–129

Geochimica et Cosmochimica Acta

www.elsevier.com/locate/gca

Equilibrium Mg isotope fractionation among aqueous Mg^{2+}, carbonates, brucite and lizardite: Insights from first-principles molecular dynamics simulations

Wenzhong Wang [a], Chen Zhou [b], Yun Liu [c], Zhongqing Wu [a,*], Fang Huang [b,*]

[a] *Laboratory of Seismology and Physics of Earth's Interior, School of Earth and Space Sciences, University of Science and Technology of China, Hefei, Anhui 230026, China*

[b] *CAS Key Laboratory of Crust-Mantle Materials and Environments, School of Earth and Space Sciences, University of Science and Technology of China, Hefei, Anhui 230026, China*

[c] *State Key Laboratory of Ore Deposit Geochemistry, Institute of Geochemistry, Chinese Academy of Sciences, Guiyang 550002, China*

Received 17 May 2018; accepted in revised form 31 January 2019; available online 6 February 2019

Abstract

Equilibrium Mg isotope fractionation properties between aqueous Mg^{2+} and minerals are the key for the applications of Mg isotopes in geochemistry. This study conducts first-principles molecular dynamics (FPMD) simulations for aqueous Mg^{2+} based on the density functional theory (DFT). Thirty-five snapshots are extracted from the FPMD trajectories after equilibration for the calculations of the reduced partition function ratio (β factor or $10^3\ln\beta$). Combining with the β factors of minerals, we found that the β factor decreases in the sequence of lizardite > brucite > aqueous Mg^{2+} > dolomite > magnesite > calcite > aragonite. Our calculations also confirm the effect of Mg concentration on the β factor of calcite, and further show that the concentration effect is negligible when Mg/(Mg + Ca) (atomic ratio hereafter) is lower than 1/32.

Our results depict significant equilibrium Mg isotope fractionations between minerals and aqueous Mg^{2+} ($10^3\ln\alpha_{minerals\text{-}Mg\_aq}$), which are dominantly controlled by the average force constant of Mg in these phases. Compared to aqueous Mg^{2+}, carbonates are enriched in light Mg isotopes but brucite and lizardite show enrichment in heavy Mg isotopes. Among all minerals, $10^3\ln\alpha_{aragonite\text{-}Mg\_aq}$ is the largest, which is up to −14‰ at 300 K. Notably, $10^3\ln\alpha_{calcite\text{-}Mg\_aq}$ is not only controlled by temperature, but also significantly affected by Mg content in calcite. $10^3\ln\alpha_{calcite\text{-}Mg\_aq}$ is negatively correlated with Mg content in calcite. The experimentally measured Mg isotope fractionations between minerals (dolomite, magnesite, brucite) and solution at equilibrium are consistent with our predicted results, showing the accurate description of FPMD simulations for aqueous Mg^{2+} and the reliability of our calculations. Overall, the calculated equilibrium Mg isotope fractionations between minerals and aqueous Mg^{2+} provide a guideline for applications of Mg isotopes in aqueous geochemical processes.

Keywords: Mg isotopes; Equilibrium fractionation; Density functional theory; First-principles molecular dynamics simulations; Aqueous Mg^{2+}; Concentration effect; Carbonates; Brucite

1. INTRODUCTION

Magnesium (Mg) is a major element widely distributed in the hydrosphere, biosphere, and the silicate Earth. It

* Corresponding author.
E-mail addresses: wuzq10@ustc.edu.cn (Z. Wu), fhuang@ustc.edu.cn (F. Huang).

https://doi.org/10.1016/j.gca.2019.01.042
0016-7037/

plays important roles in many geochemical processes, such as continental weathering, diagenetic reactions, carbonate precipitation, the recycling of subducting materials, and mantle evolution. Magnesium has three stable isotopes (^{24}Mg, ^{25}Mg, and ^{26}Mg) with the relative mass difference of 8%. With the improvement of analytical techniques, large Mg isotope fractionations have been frequently reported during the past two decades (see reviews in Teng, 2017 and references therein), which makes it a powerful tool for studies of many fundamental geochemical processes. For example, Mg isotopes have been widely applied to investigate the continental weathering (Pogge von Strandmann et al., 2008; Teng et al., 2010; Pokrovsky et al., 2011; Huang et al., 2012; Kasemann et al., 2014; Wimpenny et al., 2014a,b), the global Mg cycle (Tipper et al., 2006; Higgins and Schrag, 2010; Beinlich et al., 2014; Fantle and Higgins, 2014), paleoenvironmental reconstruction (Anbar and Rouxel, 2007; Higgins and Schrag, 2015; Husson et al., 2015), and deep carbon recycling (Yang et al., 2012; Huang et al., 2015; Liu et al., 2015; Li et al., 2016). The increasing applications of Mg isotopes in aforementioned geochemical processes urgently require the knowledge of Mg isotope equilibrium fractionations among minerals and solutions.

Experimental studies have been performed to determine the equilibrium fractionation factors of Mg isotopes between precipitated minerals and coexisting solutions (Immenhauser et al., 2010; Pearce et al., 2012; Li et al., 2012; Saulnier et al., 2012; Mavromatis et al., 2013; Wang et al., 2013; Li et al., 2014; Wimpenny et al., 2014a,b; Li et al., 2015; Mavromatis et al., 2017). However, controversies still exist among the experimental results. For instance, Li et al. (2012) found that the Mg isotope fractionation between calcite and solution ($\Delta^{26}Mg_{calcite\text{-}solution}$) varies from −2.7‰ at 277 K to −2.2‰ at 318 K, which does not depend on the precipitation rate of calcite. On the contrary, Immenhauser et al. (2010) and Mavromatis et al. (2013) observed that $\Delta^{26}Mg_{calcite\text{-}solution}$ is heavily controlled by the calcite growth rate, and smaller $\Delta^{26}Mg_{calcite\text{-}solution}$ occurs at faster calcite growth rate. In contrast to the experiment of direct precipitation of crystalline calcite, Mavromatis et al. (2017) firstly induced the formation of amorphous calcium carbonate and then transform it to the final crystalline calcite. They found that $\Delta^{26}Mg_{calcite\text{-}solution}$ ranges from −2.36‰ to −3.63‰ at 300 K. In addition, Li et al. (2014) suggested that Mg isotope fractionation between brucite and solution ($\Delta^{26}Mg_{brucite\text{-}solution}$) increases from −0.3‰ at 280 K to 0‰ at 313 K, and Wimpenny et al. (2014a,b) reported a $\Delta^{26}Mg_{brucite\text{-}solution}$ value of 0.5‰ at 323 K. These combined data show a reversal trend from negative to positive $\Delta^{26}Mg_{brucite\text{-}solution}$ values with increasing temperature, which is apparently not consistent with the general relationship between equilibrium fractionation factors and temperature.

To quantify the equilibrium Mg isotope fractionation between minerals and aqueous Mg^{2+} ($10^3\ln\alpha_{minerals\text{-}Mg\_aq}$), theoretical studies have been performed in recent years. Rustad et al. (2010) determined the dependence of $10^3\ln\alpha_{carbonates\text{-}Mg\_aq}$ on temperature using quantum chemistry calculations based on embedded clusters, which shows large disagreements with the theoretical results using the density functional theory (DFT) and periodic boundary conditions (Schauble, 2011). Recently, Pinilla et al. (2015) performed path integral molecular dynamics simulations (PIMD) based on the empirical force field and Car-Parrinello molecular dynamics (CPMD) simulations for aqueous Mg^{2+}. Specially, they selected a dozen snapshots from CPMD to calculate the β-factor of aqueous Mg^{2+} based on the DFT. For minerals, they also carried out DFT calculations but with fixed lattice parameters as experimental values. However, it is likely that this treatment produces artificial stresses for minerals in the relaxed structures, which may increase the uncertainty of the calculated results. For brucite, Colla et al. (2018) predicted that brucite should be enriched in ^{26}Mg relative to aqueous Mg^{2+}, in contrast to experimental observations (Li et al., 2014). In addition, a newly designed cluster model, volume variable cluster model, was also used to calculate $10^3\ln\alpha_{minerals\text{-}Mg\_aq}$ based on quantum chemistry method (Gao et al., 2018), which also supports the enrichment of heavy Mg isotopes in brucite. Overall, although many experimental and theoretical studies investigated Mg isotope fractionations between minerals and aqueous Mg^{2+}, there are still significant discrepancies among them.

Previous studies have proved that the equilibrium fractionation of many isotopes among crystals can be well predicted using the calculations of vibrational frequencies based on the DFT with the periodic boundary conditions (Méheut et al., 2009; Schauble, 2011; Huang et al., 2013, 2014; Feng et al., 2014; Wu et al., 2015; Qin et al., 2016; Wang et al., 2017a,b). In this study, we adopted the same strategy to calculate the β-factors of minerals. For aqueous Mg^{2+}, we firstly performed first-principles molecular dynamics (FPMD) simulations based on the DFT (Kowalski and Jahn, 2011; Dupuis et al., 2015; Pinilla et al., 2015; Ducher et al., 2018), and then extracted sufficient snapshots from the FPMD trajectories for vibrational frequencies calculations. The β factor of aqueous Mg^{2+} can be estimated from the statistical average β factor value of each selected snapshot. In this way, we provided reliable equilibrium Mg isotope fractionation data among aqueous Mg^{2+}, carbonates, brucite, and lizardite.

2. METHODS

2.1. Equilibrium mass-dependent isotope fractionation

Equilibrium isotope fractionation originates from shifts in vibrational frequencies caused by isotopic substitution of an element in a given system (Bigeleisen and Mayer, 1947; Urey, 1947), which consequently affects the vibrational partition function. According to Bigeleisen and Mayer (1947), under the harmonic approximation, the reduced partition function ratio β_A of an element X in Phase A, which represents the isotope fractionation factor between Phase A and an ideal gas of X atoms, can be expressed as:

$$\beta_A = \frac{Q_h}{Q_l} = \prod_i^{3N} \frac{u_{ih}}{u_{il}} \frac{e^{-\frac{1}{2}u_{ih}}}{1-e^{-u_{ih}}} \frac{1-e^{-u_{il}}}{e^{-\frac{1}{2}u_{il}}} \quad (1)$$

where h and l represent the heavy and light isotopes respectively; i is a running index of vibrational frequency mode,

and N is the number of atoms in the unit cell; Q_h and Q_l refer to the vibrational partition function for the heavy and light isotopes, respectively. A phase with N atoms has $3N$ vibrational modes and thus the product runs over all $3N$ phonon modes. u_{ih} and u_{il} are defined as:

$$u_{ih\ or\ il} = \hbar\omega_{ih\ or\ il}/k_B T \quad (2)$$

where $\hbar$ and k_B is the Planck and Boltzmann constants, respectively; T is temperature in Kelvin, and $\omega_{ih\ or\ il}$ is the vibrational frequency of the i^{th} mode. Following Richet et al. (1977), the equilibrium isotope fractionation between two Phases A and B can be derived in per mil (‰) as:

$$\Delta_{A-B} \approx 10^3 ln\alpha_{A-B} = 10^3 ln\beta_A - 10^3 ln\beta_B \quad (3)$$

2.2. First-principles calculations

2.2.1. First-principles molecular dynamics simulations

To obtain the structure of aqueous Mg^{2+}, we performed first-principles molecular dynamics (FPMD) simulations based on the DFT using VASP with the projector-augmented wave (PAW) method (Blöchl, 1994). To test the effect of Mg content of the aqueous solution on the structure, we performed FPMD simulations using the cubic cells containing one Mg atom and 30, 50, and 70 water molecules, respectively. Two Cl atoms were added to keep the charge balance. In addition, we also simulated the cell with one Mg atom, one Ca atom, four Cl atoms and 50 water molecules to check the effect of Ca atom on the aqueous Mg^{2+} structure. Hereafter we used the abbreviations "$1Mg30H_2O$", "$1Mg50H_2O$", "$1Mg70H_2O$", and "$1Mg1Ca50H_2O$" to represent these simulation cells, omitting all Cl atoms.

All simulations were performed in the NVT thermodynamic ensemble with the fixed temperature of 300 K, which is controlled by a Nosé thermostat. The generalised-gradient approximation (GGA) (Perdew et al., 1996) for the exchange-correlation functional was adopted and the PAW pseudopotentials were used. The energy cutoff for all calculations was 600 ev. The cell-parameter of cubic boxes set for $1Mg30H_2O$, $1Mg50H_2O$, $1Mg70H_2O$, and $1Mg1Ca50H_2O$ are 9.9544, 11.5600, 12.7950, 11.9700 Å respectively, to ensure the simulated statistical pressure of approximately zero kbar (Fig. S3) and the experimental density of ~1 g/cm^3. For all FPMD simulations, the time step was set to be 1 fs, and the total running time is up to 45 ps. The Brillouin zone summations over the electronic states were performed at gamma point.

2.2.2. Phonon vibration frequency calculations

For Mg^{2+} aqueous solutions, we extracted 35 snapshots from the FPMD trajectories every 1000 steps after equilibration, and optimized their atomic positions with fixed cubic boxes. For carbonates, brucite, and lizardite, their cell parameters and atomic positions were well relaxed with the k-point grid mesh dependent on the size of unit cells (Table S1) at ambient pressure. For all structure optimizations, the residual forces converge within 10^{-3} ev/Å. In order to estimate the β factor of $^{26}Mg/^{24}Mg$ for all phases, we performed full calculations of phonon vibration frequencies using the finite displacement method as implemented in the open-source code PHONOPY (Togo and Tanaka, 2015).

3. RESULTS

3.1. Structures of carbonates, brucite, lizardite, and aqueous Mg^{2+}

The conventional cell of calcite is a 30-atom crystal containing six symmetry-equivalent Ca atoms. The initial crystal structures of calcite with variable Mg concentrations were obtained by replacing Ca atoms with Mg atoms in the supercells of calcite. For instance, a series of calcite with Mg/(Mg + Ca) (mole ratio hereafter) of 1/24, 2/24, and 4/24 were generated by substituting one, two, and four Ca atoms with Mg atoms in the 120-atom supercell of calcite, respectively. The supercell was constructed by expanding the conventional cell twice times along both of a and b directions. Similarly, we separately expanded the conventional cell of calcite twice along a, b, and c directions to obtain the 240-atom supercell, and then substituted one Ca atom with one Mg atom to create the structure of calcite with Mg/(Mg + Ca) of 1/48. In addition, one Ca atom was replaced by one Mg atom in the 160-atom and 240-atom supercells of aragonite to yield the initial structures of aragonite with Mg/(Mg + Ca) of 1/32 and 1/48, respectively. Because there are more than one configurations for the initial structures of calcite with Mg/(Mg + Ca) of 2/24 and 4/24, all nonequivalent configurations for these Mg-bearing calcite were calculated and the configurations with the lowest total energy (Fig. S1) were selected for the vibrational frequency calculations.

The calculated volumes of carbonates, brucite, and lizardite within GGA are ~3% larger than experimental data at ambient pressure (Table S1), whereas LDA predicts a bit smaller volumes of Mg-bearing calcite (Wang et al., 2017a). It is typical that LDA underestimates but GGA overestimates the equilibrium volume (Wentzcovitch et al., 2010; Schauble, 2011; Wang and Wu, 2018). Average Mg-O bond lengths in these solids are reported in Table 1. All Mg atoms in calcite-type carbonates, brucite, and lizardite have a coordination number (CN) of six, while the CN of Mg atom in aragonite is nine if the cutoff of the Mg-O bond length is set as 3 Å. Among these Mg-bearing minerals, the average Mg-O bond length is the shortest in lizardite but the longest in aragonite. Because the volume of Ca-O polyhedron in aragonite is much larger than that in calcite, it is expected that aragonite has much longer average Mg-O bond length compared to calcite when Mg atom is incorporated into the Ca site. The average Mg-O bond length increases in the order of lizardite < brucite ~ dolomite < magnesite < calcite < aragonite. Wang et al. (2017a) found that the average Mg-O bond length sharply increases with decreasing Mg/(Mg + Ca) in calcite from 3/6 to 1/12. Our calculations within the GGA also support the concentration effect on the average Mg-O bond length in calcite with Mg/(Mg + Ca) varying from 3/6 to 1/24 (Table 1 and Fig. 3a), although the absolute values in this

Table 1
Average Mg-O bond lengths in carbonates, brucite, and lizardite.

Minerals	Chemical formula	Mg/(Mg + Ca)	Average Mg-O bond length (Å)	
			This study	Wang et al. (2017a,b)
Calcite	$MgCa_{47}C_{48}O_{144}$	1/48	2.169	
	$MgCa_{23}C_{24}O_{72}$	1/24	2.167	
	$Mg_2Ca_{22}C_{24}O_{72}$	2/24	2.152	2.093*
	$Mg_4Ca_{20}C_{24}O_{72}$	4/24	2.124	2.074†
Dolomite	$Mg_3Ca_3C_6O_{18}$	3/6	2.103	2.057
Magnesite	$Mg_6C_6O_{18}$	6/6	2.120	2.076
Aragonite	$MgCa_{47}C_{48}O_{144}$	1/48	2.317	
	$Mg\ Ca_{31}C_{32}O_{96}$	1/32	2.320	
Brucite	$Mg(OH)_2$	–	2.106	
Lizardite	$Mg_3Si_2O_5(OH)_4$	–	2.088	

Data in Wang et al. (2017a,b).
* Mg/(Mg + Ca) = 1/12.
† Mg(Mg + Ca) = 1/6.

study are obviously larger than those calculated within the LDA (Wang et al., 2017a). This is principally because the GGA predicts a much larger volume than the LDA (Table S1). However, the relative variations in the average Mg-O bond length are consistent with the predictions within the LDA (Wang et al., 2017a). For example, both of the GGA and LDA predict an increase of ~0.018 Å in the average Mg-O bond length when Mg/(Mg + Ca) decreases from 4/24 to 2/24. In particular, our results show that, when Mg/(Mg + Ca) in calcite decreases from 1/24 to 1/48, the average Mg-O bond length only slightly increases from 2.166 to 2.169 Å. This implies that the average Mg-O bond length in calcite is sensitive to Mg concentration only when Mg/(Mg + Ca) ranges from 3/6 to 1/24, similar to the behavior of the average Ca-O bond length in orthopyroxene (Feng et al., 2014; Wang et al., 2017b). Notably, the average Mg-O bond length in aragonite only slightly changes when Mg/(Mg + Ca) varies from 1/32 to 1/48, indicating that the effect of Mg concentration is negligible when Mg/(Mg + Ca) is lower than 1/32.

The structure of aqueous Mg^{2+} is not set as solids, but under an equilibrium state of flux. To assess the structural properties of aqueous Mg^{2+}, we calculated the partial radial distribution function (PRDF) (Liu et al., 2018) between Mg and O, which can be expressed as:

$$g_{Mg-O}(r) = \frac{N}{\rho N_{Mg} N_O} \langle \sum_{i=1}^{N_{Mg}} \sum_{j=1}^{N_O} \delta\left(\vec{r} - \vec{R}_i^{Mg} + \vec{R}_j^{O}\right) \rangle \quad (4)$$

where ρ is the atomic number density, and N is the total number of atoms. N_{Mg} and N_O refer to the number of Mg and O atoms, respectively. $\vec{R}$ represents the coordinates of atoms. The PRDFs of Mg-O pair in all aqueous solutions show very sharp peaks at ~2.08 Å (Fig. 1a), suggesting strong Mg-O bonds in liquids. The peak position of PRDF of $1Mg30H_2O$ locates at a smaller value than these of $1Mg50H_2O$, $1Mg70H_2O$, and $1Mg1Ca50H_2O$, which have almost an identical peak position (Fig. 1a). These results reveal the stronger Mg-O interaction in $1Mg30H_2O$ and that the structure of aqueous Mg^{2+} will not be significantly affected by the number of water molecules (or Mg content) in aqueous models when it is more than 50. In addition, the calculated CNs of aqueous Mg^{2+} using the PRDFs in all solutions sharply increase from 0 to 6 when the cutoff of Mg-O distance increases from 1.8 to 2.4 Å, consistent with the sharp distribution of Mg-O within this

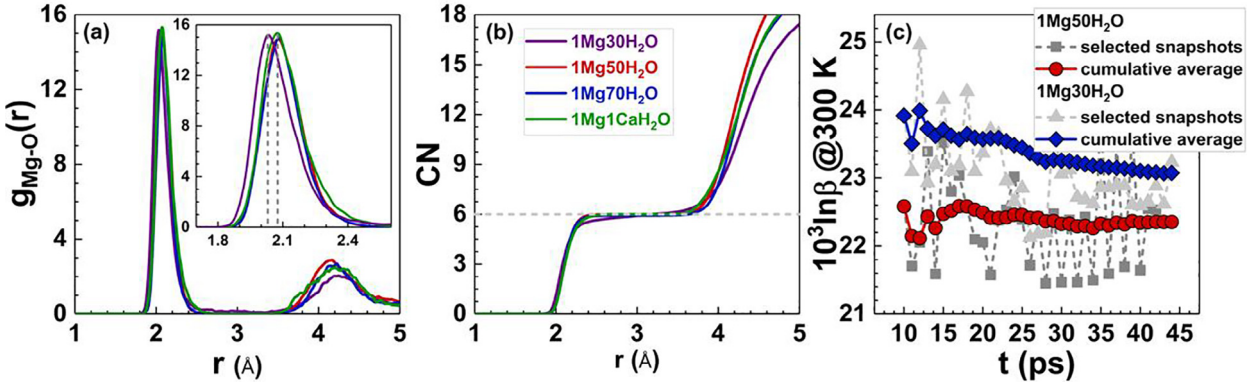

Fig. 1. (a) Radial distribution functions g(r) for M-O pair. (b) Coordination numbers (CNs) of aqueous Mg^{2+}. (c) The reduced partition function ratios ($10^3 ln\beta$) of $^{26}Mg/^{24}Mg$ of the selected snapshots for $1Mg50H_2O$ and $1Mg30H_2O$ and their cumulative averages in the time domain at 300 K.

range. The predicted hydration number around Mg^{2+} is well consistent with experimental measurements (Ohtaki and Radnai, 1993 and references therein). On the other hand, the radial distribution functions for Mg-Cl pairs in aqueous solutions show that there is no direct chemical bonding between Mg and Cl atoms in the first Mg-O solvation shells (Fig. S2).

3.2. Reduced partition function ratios of $^{26}Mg/^{24}Mg$

We extracted 35 snapshots from the FPMD trajectories of $1Mg30H_2O$ and $1Mg50H_2O$ every 1000 steps after equilibration for the full vibrational frequency calculations, and their reduced partition function ratios ($10^3\ln\beta$) of $^{26}Mg/^{24}Mg$ at 300 K are reported in Fig. 1c. Although $10^3\ln\beta$ of both aqueous solutions are obviously scattered in the time domain, their cumulative averages gradually evolve to be constant values when more than 25 continuous snapshots are included. The more snapshots are included, the more reliable the statistical average of $10^3\ln\beta$ is, and clearly the more computations are required. Our results show that the statistical average on 35 snapshots is an excellent representative for aqueous Mg^{2+} and the statistical error of $10^3\ln\beta$ is small ($< 0.6\%$, e.g., $10^3\ln\beta$ of $1Mg50H_2O$ is $22.35 \pm 0.12‰$ at 300 K). It is also noteworthy that $1Mg30H_2O$ has a larger statistical average of $10^3\ln\beta$ than $1Mg50H_2O$, because the Mg-O distances of $1Mg30H_2O$ are systematically smaller than those of $1Mg50H_2O$ (Fig. 1a). Here we did not sample the FPMD trajectories of $1Mg70H_2O$ and $1Mg1Ca50H_2O$ due to the highly demanded computations. Because their PRDFs are almost identical to that of $1Mg50H_2O$ (Fig. 1a), we can expect that aqueous Mg^{2+} in these two solutions should have a similar $10^3\ln\beta$ to that of $1Mg50H_2O$.

The calculated temperature dependences of $10^3\ln\beta$ of aqueous Mg^{2+}, carbonates, brucite, and lizardite are shown in Fig. 2a, and their polynomial fitting parameters are reported in Table 2. $10^3\ln\beta$ decreases in the sequence of lizardite > brucite > $1Mg30H_2O$ > $1Mg50H_2O$ > dolomite > magnesite > calcite > aragonite. Compared with aqueous Mg^{2+}, the two hydroxyl minerals (lizardite and brucite) are enriched in heavy Mg isotopes, while carbonates are enriched in light Mg isotopes. Among carbonates, aragonite and dolomite have the lowest and highest $^{26}Mg/^{24}Mg$ respectively, which corresponds to the longest Mg-O bond length in aragonite and the shortest Mg-O bond length in dolomite (Table 1). The relative order of dolomite > magnesite > calcite is also supported by previous theoretical results (Rustad et al., 2010; Schauble, 2011; Wang et al., 2017a). In addition, based on the LDA calculations, Wang et al. (2017a) found that $10^3\ln\beta$ of calcite sharply decreases with Mg content because the average Mg-O bond length in calcite dramatically increases with the decrease of Mg/(Mg + Ca). Here our GGA calculations also confirm this negative

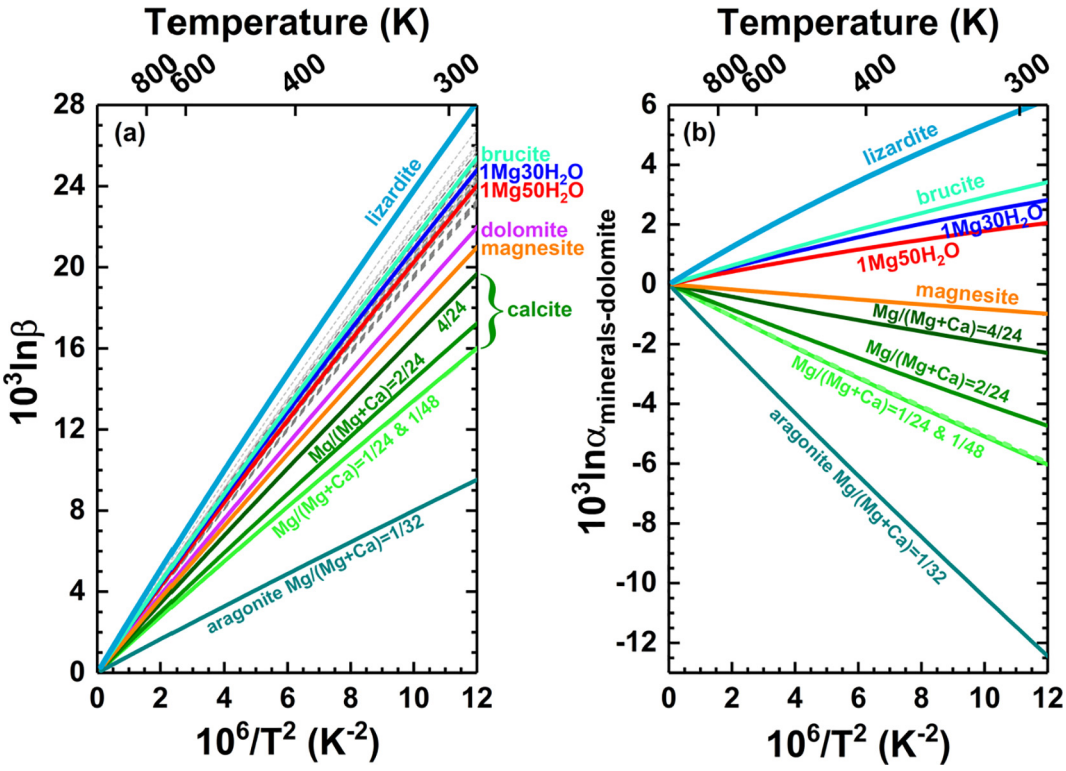

Fig. 2. (a) The reduced partition function ratios ($10^3\ln\beta$) of $^{26}Mg/^{24}Mg$ of aqueous Mg^{2+}, carbonates, brucite, and lizardite. (b) The equilibrium Mg isotope fractionation ($10^3\ln\alpha$) between dolomite and others (aqueous Mg^{2+}, calcite, aragonite, brucite, and lizardite). Light grey short dash and dark grey dash lines represent 35 snapshots of $1Mg30H_2O$ and $1Mg50H_2O$ respectively, and blue and red solid lines correspond to their statistical averages. The statistical errors associated with $10^3\ln\beta$ of aqueous Mg^{2+} are ~0.12% at 300 K. (For interpretation of the references to colour in this figure legend, the reader is referred to the web version of this article.)

Table 2
Polynomial fitting parameters of the reduced partition function ratios ($10^3\ln\beta$) of $^{26}Mg/^{24}Mg$ with temperature for aqueous Mg^{2+}, carbonates, brucite, and lizardite.

Phase	Mg/(Mg + Ca)	Force constant of Mg (N/m)	a	b	c
$1Mg50H_2O$	–	157.20	2.16717	−0.01681	2.51E−04
$1Mg30H_2O$	–	162.09	2.23682	−0.01682	2.13E−04
Calcite	1/48	99.86	1.39862	−0.00741	1.26E−04
	1/24	100.32	1.40511	−0.00742	1.26E−04
	2/24	108.09	1.51431	−0.00806	1.30E−04
	4/24	123.57	1.73298	−0.00949	1.40E−04
Dolomite	3/6	138.42	1.94215	−0.01118	1.55E−04
Magnesite	6/6	132.37	1.85657	−0.01099	1.65E−04
Aragonite	1/32	60.77	0.84303	−0.00556	1.21E−04
Brucite	–	163.13	2.26569	−0.01423	1.44E−04
Lizardite	–	187.03	2.59910	−0.02665	4.62E−04

Polynomial fitting equation: $10^3\ln\beta = ax + bx^2 + cx^3$, where $x = 10^6/T^2$. T is temperature in Kelvin. All polynomial fittings are performed between 270 K and 1500 K.

dependence of $10^3\ln\beta$ of calcite on Mg/(Mg + Ca), although the absolute values of $10^3\ln\beta$ are systematically larger than those in Wang et al. (2017a). This is mainly because different approximations were adopted in the first-principles calculations (LDA VS. GGA). These systematical variations were also found in previous calculations on $10^3\ln\beta$ of $^{26}Mg/^{24}Mg$ of mantle minerals (Schauble, 2011; Huang et al., 2013).

4. DISCUSSION

4.1. Concentration effect on equilibrium Mg isotope fractionation

Based on first-principles calculations within the LDA, Wang et al. (2017a) found that the average Mg-O bond length in calcite-type carbonates sharply increases with the decreasing of Mg/(Mg + Ca) when it ranges from 3/6 to 1/12. Because equilibrium Mg isotope fractionation between calcite and dolomite ($10^3\ln\alpha_{calcite\text{-}dolomite}$) is linearly correlated with the average Mg-O bond length, $10^3\ln\alpha_{calcite\text{-}dolomite}$ significantly decreases with the decrease of Mg/(Mg + Ca). Our GGA calculations also confirm the negative dependence of average Mg-O bond length in calcite-type carbonates when Mg/(Mg + Ca) in carbonates ranges from 3/6 to 1/24 (Fig. 3a), causing the positive correlation between $10^3\ln\alpha_{calcite\text{-}dolomite}$ and Mg/(Mg + Ca) (Fig. 3b), which is almost identical to the calculated results within LDA (Wang et al., 2017a). In contrast, when Mg/(Mg + Ca) in calcite drops from 1/24 to 1/48, the average Mg-O bond length and $10^3\ln\alpha_{calcite\text{-}dolomite}$ show subtle changes, implying that Mg concentration effect on $10^3\ln\alpha_{calcite\text{-}dolomite}$ is significant only within a certain range of Mg content in calcite (i.e., 1/24 < Mg/(Mg + Ca) < 3/6). When Mg content in calcite is low enough (i.e., Mg/(Mg + Ca) < 1/24), because the variation of chemical bonding environment around Mg atom is local and limited,

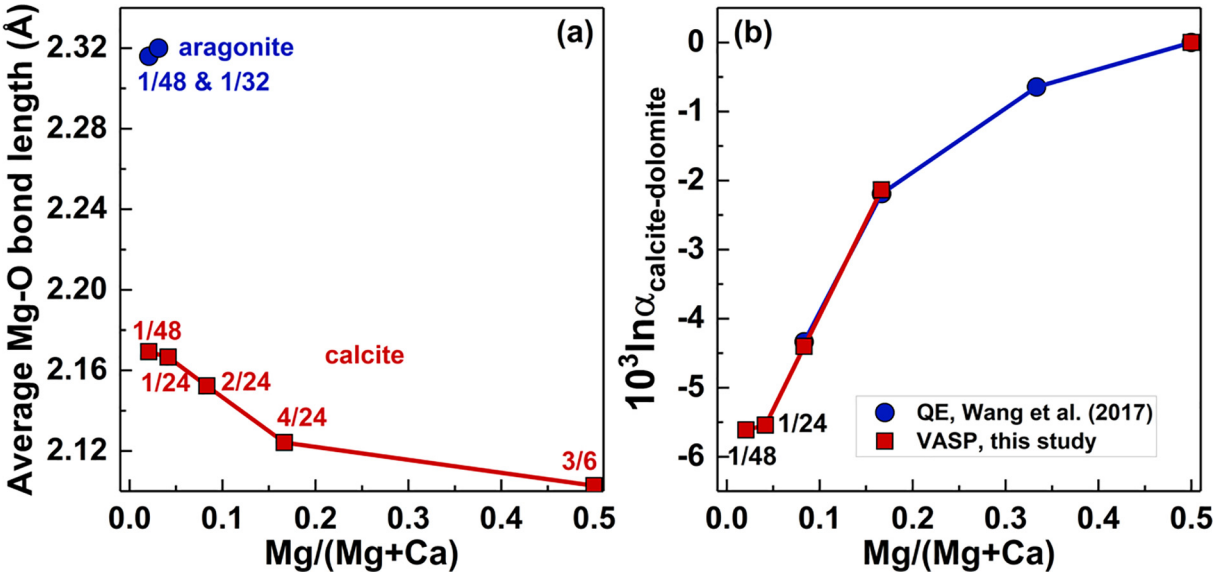

Fig. 3. (a) Average M-O bond length versus Mg/(Mg + Ca) in carbonates. (b) The equilibrium Mg isotope fractionation ($10^3\ln\alpha$) between calcite and dolomite at 300 K versus Mg/(Mg + Ca) in calcite.

$10^3\ln\alpha_{calcite\text{-}dolomite}$ reaches a constant value and does not change with Mg content. Because the average Mg-O bond length in aragonite with Mg/(Mg + Ca) of 1/48 is almost identical to that with Mg/(Mg + Ca) of 1/32, we can expect that $10^3\ln\alpha_{aragonite\text{-}dolomite}$ does not change with Mg content in aragonite when Mg/(Mg + Ca) is lower than 1/32, suggesting that the threshold Mg concentration for aragonite could be >1/32. Similarly, Wang et al. (2017b) found that $10^3\ln\alpha$ of $^{44}Ca/^{40}Ca$ between orthopyroxene and clinopyroxene is not sensitive to Ca content in orthopyroxene when Ca content is lower than 1/48. Therefore, it should be a ubiquitous phenomenon in solid solutions that the concentration effect on $10^3\ln\alpha$ is negligible if the concentration is below the threshold.

Recently, Pinilla et al. (2015) theoretically predicted that calcite with 3.12 mol% Mg is enriched in heavy Mg isotopes relative to the one with 6.25 mol% Mg based on the first-principles calculations. However, according to our results, because the Mg content of 6.25 mol% is higher than the threshold Mg concentration for calcite (1/24), $10^3\ln\beta$ of $^{26}Mg/^{24}Mg$ of calcite with 6.25 mol% Mg should be evidently larger than that with 3.12 mol% at the same temperature. This discrepancy may originate from their structure optimizations, in which the cell parameters of calcite were fixed to the experimental values. In this case, minerals were actually simulated under different pressures, and this could change their relative values of $10^3\ln\beta$ because increasing pressure significantly increases $10^3\ln\beta$ (Huang et al., 2013, 2014; Wu et al., 2015).

4.2. Controlling factors on equilibrium Mg isotope fractionation

Equilibrium isotope fractionations are mainly controlled by relevant differences between bond strengths (Bigeleisen and Mayer, 1947; Urey, 1947), which could be roughly measured by chemical bond lengths and CNs. In general, based on analysis from previous studies (Schauble et al., 2004; Hill and Schauble, 2008; Young et al., 2009; Huang et al., 2013, 2014; Wang et al., 2017a,b), shorter chemical bonds have higher vibrational frequencies corresponding to stronger bond strengths, and thus are enriched in heavy isotopes compared to longer ones. Our calculated results also suggest that $10^3\ln\beta$ of $^{26}Mg/^{24}Mg$ of calcite-type carbonates are linearly correlated with their average Mg-O bond lengths (Fig. 4a), while the data of aragonite and two hydroxyl minerals deviate from this linear relationship. Specially, dolomite has a similar average Mg-O bond length and identical CN relative to brucite (Table 1), whereas $10^3\ln\alpha$ between brucite and dolomite is up to 3.2‰ at 300 K (Fig. 4a).

In order to figure out the controlling factors on the large equilibrium Mg isotope fractionations among these phases, we calculated the average force constant of Mg $\langle F\rangle$ (in N/m) (Table 2) from the partial phonon density of state $g(E)$ of Mg following the equation (Dauphas et al., 2012):

$$\langle F\rangle = \frac{M}{\hbar^2}\int_0^{+\infty} E^2 g(E)dE \quad (5)$$

As shown in Fig. 4b, $10^3\ln\beta$ of $^{26}Mg/^{24}Mg$ at 300 K are linearly correlated with $\langle F\rangle$ of Mg, including both minerals and the aqueous Mg^{2+}. A larger $\langle F\rangle$ corresponds to a higher value of $10^3\ln\beta$ and thus the enrichment of heavy Mg isotopes relative to a smaller one (Ducher et al., 2018). Although brucite and dolomite have almost identical average Mg-O bond lengths, the large $10^3\ln\alpha$ between them can be explained by the relative difference in $\langle F\rangle$ value, which also reveals the intensity of interactions between Mg atoms and other atoms including the nearby O atoms. Similarly, the much smaller $\langle F\rangle$ value of Mg in aragonite compared to other phases clearly illustrates that aragonite

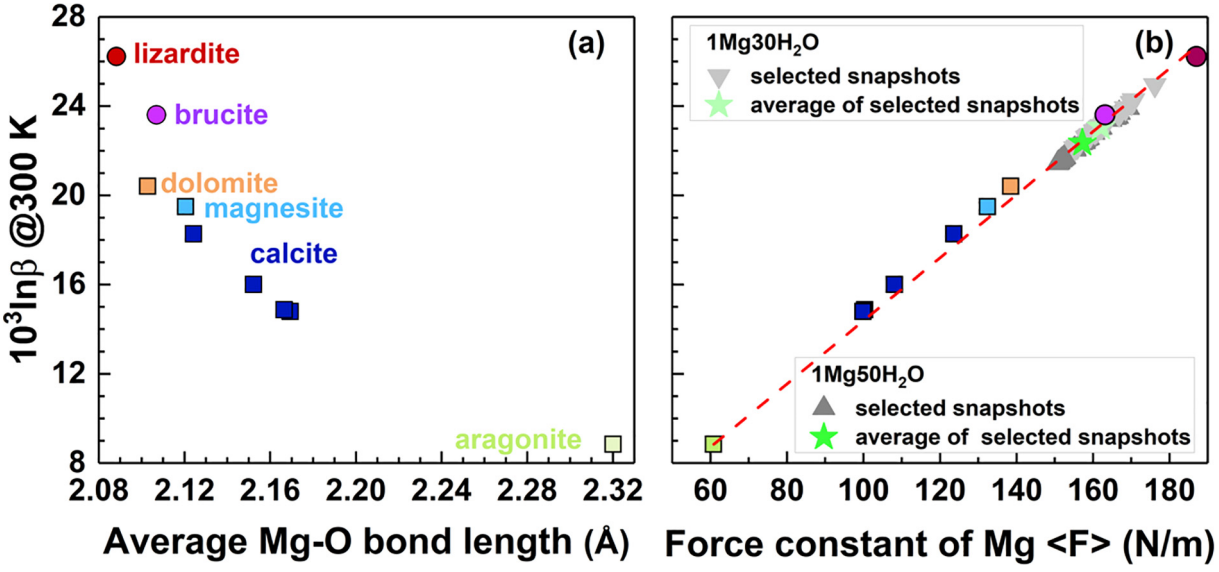

Fig. 4. $10^3\ln\beta$ of $^{26}Mg/^{24}Mg$ at 300 K versus (a) average Mg-O bond length (b) Force constant of Mg in aqueous Mg^{2+}, calcite, aragonite, brucite, and lizardite.

should be enriched in light Mg isotopes (Fig. 4b). Furthermore, the $\langle F \rangle$ value of Mg in calcite decreases with decreasing Mg/(Mg + Ca) from 3/6 to 1/24, and then remains constant when Mg/(Mg + Ca) drops from 1/24 to 1/48. Therefore, the variation in Mg contents changes the interactions between Mg atom and other atoms, which further significantly affect the force constant of Mg atom. When Mg content is low enough, these interactions gradually evolve to be constant, because chemical environment around Mg atom will not change anymore. This explains the existence of the threshold of Mg concentration below which the $10^3\ln\alpha$ is insensitive to Mg content.

4.3. Equilibrium Mg isotope fractionation between minerals and aqueous Mg^{2+}

Carbonates (such as calcite, aragonite, dolomite, and magnesite) are common components of sediments and provide important records on many fundamental geochemical processes. Mg isotope data in carbonates have been widely applied to investigate the Mg global cycle (Tipper et al., 2006; Higgins and Schrag, 2010; Beinlich et al., 2014; Fantle and Higgins, 2014) and paleo-environmental reconstruction (Anbar and Rouxel, 2007; Higgins and Schrag, 2015; Husson et al., 2015). The equilibrium Mg isotope fractionation factors between carbonates and aqueous Mg^{2+} ($10^3\ln\alpha_{carbonates\text{-}Mg\_aq}$) are the key parameters for these applications. Here we calculated $10^3\ln\alpha_{carbonates\text{-}Mg\_aq}$ of $^{26}Mg/^{24}Mg$ from the corresponding $10^3\ln\beta$ (Fig. 5) and reported their polynomial fitting parameters with temperature in Table 3.

4.3.1. Dolomite vs. aqueous Mg^{2+}

For dolomite and aqueous Mg^{2+}, Li et al. (2015) for the first time calibrated the equilibrium Mg isotope fractionation between dolomite and solution, varying from −0.93‰ at 403 K to −0.65‰ at 493 K. In their experiments, the complete isotope exchange at high temperature between dolomite and solution was proved using ^{25}Mg and Sr isotope tracers. Our calculated results agree well with these experimental measurements at high temperature (Fig. 5a). The $10^3\ln\alpha_{dolomite\text{-}Mg\_aq}$ is -1.94 ± 0.27‰ at 300 K (Fig. 5a), in contrast to other theoretical studies (Rustad et al., 2010; Schauble, 2011; Gao et al., 2018), in which $10^3\ln\alpha_{dolomite\text{-}Mg\_aq}$ significantly deviates from the experimental results and varies from a negative to positive value (Fig. 5a). The uncertainty of $10^3\ln\alpha$ in this study is estimated by combining the statistical error of aqueous Mg^{2+} (e.g., 0.12‰ at 300 K) with the one caused by a ~5% error for calculated vibrational frequencies of minerals (Gao et al., 2018), which results in ~8% error for $10^3\ln\alpha$ (Méheut et al., 2009). Although the estimated $10^3\ln\alpha_{dolomite\text{-}Mg\_aq}$ in Pinilla et al. (2015) are consistent with our results and experimental data within their uncertainties, it is important to note that the error for $10^3\ln\alpha_{dolomite\text{-}Mg\_aq}$ in Pinilla et al. (2015) is up to 2.0‰, even larger than the measured fractionation in Li et al. (2015). This implies the importance of FPMD simulations for aqueous Mg^{2+}, which has no regular structure as crystals and probably cannot be simply represented by one cluster model. Schauble (2011) calculated $10^3\ln\beta$ of six salts containing the $Mg(H_2O)_6^{2+}$ solvation complex based on the DFT and periodic boundary conditions, and then used the average value to represent the $10^3\ln\beta$ of aqueous Mg^{2+}. However, according to our results, $10^3\ln\beta$ of brucite and lizardite containing hydroxyl are larger than that of aqueous Mg^{2+} at the same temperature (Fig. 3a), suggesting that the $10^3\ln\beta$ of aqueous Mg^{2+} in Schauble (2011) may be overestimated and thus the negative $10^3\ln\alpha_{dolomite\text{-}Mg\_aq}$ is also overestimated. Pinilla et al. (2015) also performed the CPMD simulations for aqueous Mg^{2+}, but their mineral structures were relaxed with the fixed cell parameters as experimental values, which result in the structures under different external pressures. To check the effect of this treatment, we also only relaxed the atomic positions of dolomite with fixed experimental cell parameters and found that the relaxed structure is actually under ~2.8 GPa. Consequently, the calculated $10^3\ln\beta$ at 300 K increases from 20.41‰ to 22.78‰ and $10^3\ln\alpha_{dolomite\text{-}Mg\_aq}$ changes from −1.94‰ to 0.43‰. This well explains the calculated $10^3\ln\alpha_{dolomite\text{-}Mg\_aq}$ of ~0.4 ± 0.5‰ in Pinilla et al. (2015), which was estimated by relaxing the atomic positions of snapshots from the FPMD trajectories (named "AI-RELAX"). Similarly, $10^3\ln\beta$ of other carbonates in Pinilla et al. (2015) may be also significantly overestimated.

4.3.2. Magnesite vs. aqueous Mg^{2+}

For magnesite and aqueous Mg^{2+}, Pearce et al. (2012) found that Mg isotope fractionation between magnesite and co-existing solution ($\Delta^{26}Mg_{magnesite\text{-}solution}$) at equilibrium is −1.20‰ at 423 K and −0.88‰ at 473 K. Schott et al. (2016) also reported $\Delta^{26}Mg_{magnesite\text{-}solution}$ of −1.10‰ at 423 K and −0.72‰ at 473 K on average. These fractionation data from Pearce et al. (2012) are close to but systematically ~0.3‰ smaller than our results (−1.21 ± 0.14‰ at 473 K and −1.53 ± 0.14‰ at 423 K). As mentioned above, because the $10^3\ln\beta$ of aqueous Mg^{2+} in Schauble (2011) and magnesite in Pinilla et al. (2015) were overestimated, the negative $10^3\ln\alpha_{magnesite\text{-}Mg\_aq}$ from Schauble (2011) is much larger and the value in Pinilla et al. (2015) is much smaller than our calculations, respectively. Schott et al. (2016) found that Mg^{2+}-bearing species other than aqueous Mg^{2+} (e.g., $MgHCO_3^+$, $MgCO_3^\circ$) in the solution have higher $10^3\ln\beta$ than that of aqueous Mg^{2+} based on embedded-cluster-based quantum chemistry calculations. They consequently suggested that the measured negative $\Delta^{26}Mg_{magnesite\text{-}solution}$ (−1.10‰ at 423 K and −0.72‰ at 473 K on average) should be larger than that between magnesite and aqueous Mg^{2+}, which was ~−0.73‰ at 423 K and ~−0.43‰ at 473 K on average. These values are close to the predictions from Gao et al. (2018) and Pinilla et al. (2015) within the large uncertainty of ~1.5‰ but significantly deviates from our results. Further studies are needed to resolve this controversy.

4.3.3. Calcite vs. aqueous Mg^{2+}

For calcite and aqueous Mg^{2+}, Li et al. (2012) found that the Mg isotope fractionation between calcite and solution ($\Delta^{26}Mg_{calcite\text{-}solution}$) varies from −2.7‰ at 277 K to

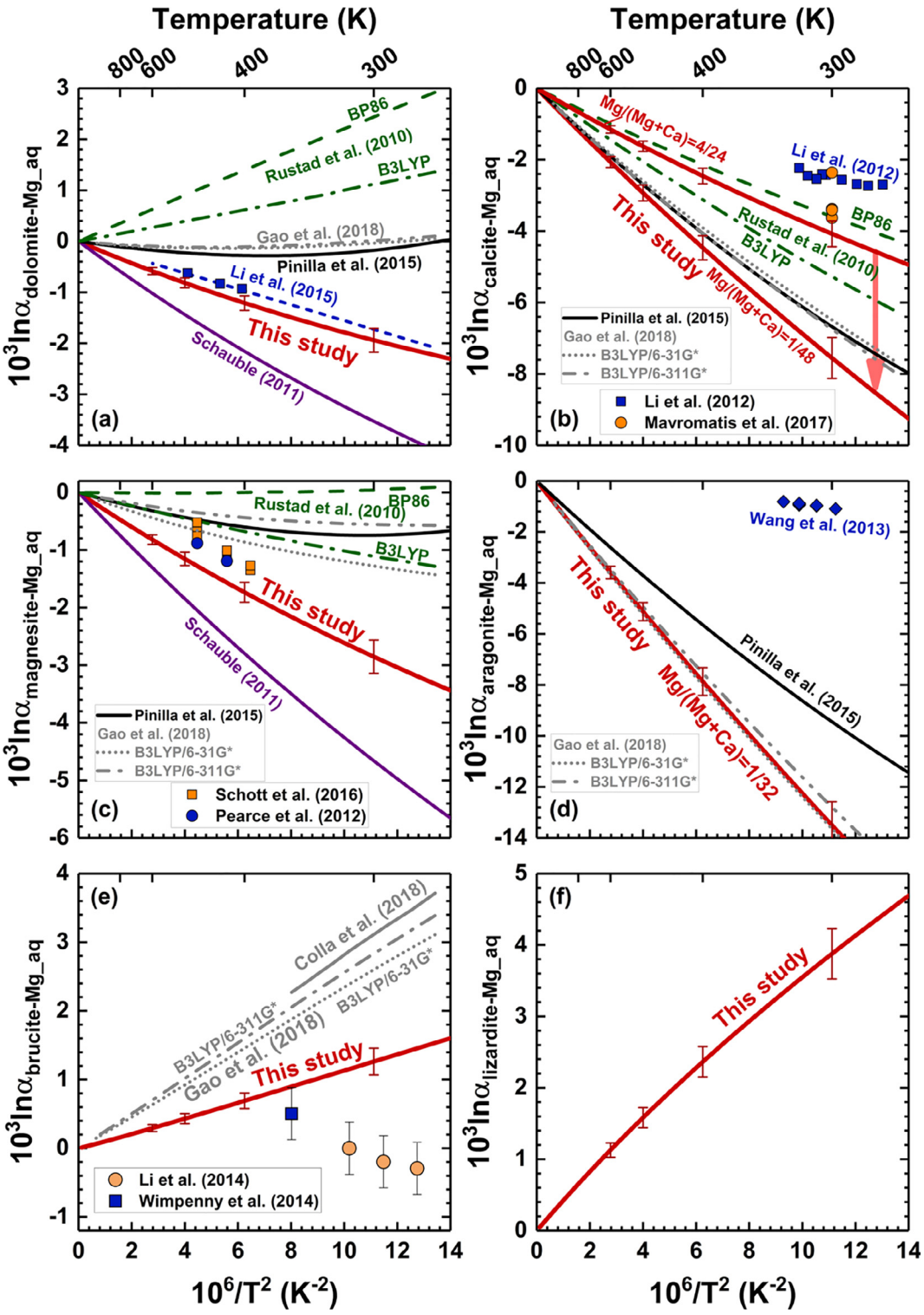

Fig. 5. The temperature dependent equilibrium Mg isotope fractionation ($10^3 ln\alpha$) between mineral (dolomite, calcite, magnesite, aragonite, brucite, and lizardite) and aqueous Mg^{2+}. Error bars have been estimated by combining the statistical error bar of aqueous Mg^{2+} with the uncertainty produced by the error of the calculated vibrational frequencies (~5%) (Gao et al., 2018).

−2.2‰ at 318 K, which does not depend on the precipitation rate. However, Immenhauser et al. (2010) and Mavromatis et al. (2013) observed that $\Delta^{26}Mg_{calcite\text{-}solution}$ is heavily controlled by the calcite growth rate with smaller $\Delta^{26}Mg_{calcite\text{-}solution}$ occurring at the faster calcite growth rate. In addition, other factors, such as aqueous Mg

Table 3
Polynomial fitting parameters of the equilibrium Mg isotope fractionation ($10^3\ln\alpha$) with temperature between aqueous Mg^{2+} ($1Mg50H_2O$) and minerals (carbonates, brucite, and lizardite).

Phase	Mg/(Mg + Ca)	a	b	c
Calcite	1/48	−0.76855	0.00940	−1.25E−04
	1/24	−0.76206	0.00939	−1.25E−04
	2/24	−0.65286	0.00875	−1.21E−04
	4/24	−0.43419	0.00732	−1.11E−04
Dolomite	3/6	−0.22502	0.00563	−9.60E−05
Magnesite	6/6	−0.31060	0.00582	−8.60E−05
Aragonite	1/32	−1.32414	0.01125	−1.30E−04
Brucite	–	0.09852	0.00258	−1.07E−04
Lizardite	–	0.43193	−0.00984	2.11E−04

Polynomial fitting equation: $10^3\ln\alpha_{minerals\text{-}Mg\_aq} = 10^3\ln\beta_{minerals}$-$10^3\ln\beta_{Mg\_aq} = ax + bx^2 + cx^3$, where $x = 10^6/T^2$. T is temperature in Kelvin. All polynomial fittings are performed between 270 K and 1500 K.

concentration, pH, and the precipitation process, may also influence Mg isotope fractionation (Saenger and Wang, 2014). Our results further show that, $10^3\ln\alpha_{calcite\text{-}Mg\_aq}$ is not only controlled by temperature, but also significantly affected by Mg content in calcite (Fig. 5b). Larger negative $10^3\ln\alpha_{calcite\text{-}Mg\_aq}$ occurs at lower Mg content in calcite. When Mg/(Mg + Ca) = 4/24, the $10^3\ln\alpha_{calcite\text{-}Mg\_aq}$ is -4.00 ± 0.44‰ at 300 K. In contrast to the experiments of direct precipitation of crystalline calcite, Mavromatis et al. (2017) firstly induced the formation of amorphous calcium carbonate (ACC) and then transform it to the final crystalline calcite. They found that $\Delta^{26}Mg_{calcite\text{-}solution}$ at the approach of isotopic exchange equilibrium ranges from −2.36‰ to −3.63‰, which depends on Mg content in calcite. Notably, the measured $\Delta^{26}Mg_{calcite\text{-}solution}$ is quite close to our calculated results when calcite has a high Mg content. However, it was suggested that the decrease of Mg content in calcite shifts $\Delta^{26}Mg_{calcite\text{-}solution}$ to a smaller negative value (Mavromatis et al., 2017), contrary to our predicted Mg concentration effect on $10^3\ln\beta$ of calcite (Wang et al., 2017a). Variations in aqueous Mg^{2+} concentration cannot account for this discrepancy, because the PRDF of Mg-O almost does not change with Mg^{2+} concentration when it is low enough (Fig. 1a). Previous studies suggested that the ACC-calcite transformation is a dissolution–repre cipitation process (Giuffre et al., 2015; Purgstaller et al., 2016). It is possible that, as Gao et al. (2018) speculated, the rapid transformation from ACC to calcite within 25–60 minutes in the experiment of Mavromatis et al. (2017) may not reach the chemical equilibrium state.

4.3.4. Aragonite vs. aqueous Mg^{2+}

For aragonite and aqueous Mg^{2+}, our calculated equilibrium fractionation is up to -14.00 ± 1.24‰ at 300 K, much larger than the experimental measurements (−1.09‰ at 300 K) (Wang et al., 2013). It is noteworthy that the large negative $10^3\ln\alpha_{aragonite\text{-}Mg\_aq}$ predicted in this study is self-consistent with the great differences of $\langle F \rangle$ between aragonite and aqueous Mg^{2+}. Using the molecular dynamics simulations based on empirical potentials, Ruiz-Hernandez et al. (2012) found that Mg is preferentially incorporated in surfaces rather than the bulk of aragonite, and the Mg-O distance in the most favorable surface of aragonite is only slightly longer than that of aqueous Mg^{2+} (about 2.08 Å versus 2.05 Å). This consequently leads to a rather small Mg isotope fractionation between Mg incorporated in the aragonite surfaces and aqueous Mg^{2+}, which may explain the big discrepancy between theoretical and experimental studies (−14.0‰ vs. −1.09‰ at 300 K).

4.3.5. Brucite and lizardite vs. aqueous Mg^{2+}

Brucite is an important mineral that occurs in the chemical weathering and serpentinization. The equilibrium Mg isotope fractionation between brucite and aqueous Mg^{2+} ($10^3\ln\alpha_{brucite\text{-}Mg\_aq}$) is important for the application of Mg isotopes in the continental weathering. Our calculated results show that $10^3\ln\alpha_{brucite\text{-}Mg\_aq}$ is always positive at varying temperatures (Fig. 5e), suggesting the enrichment of ^{26}Mg in brucite relative to aqueous Mg^{2+}. $10^3\ln\alpha_{brucite\text{-}Mg\_aq}$ varies from 1.26 ± 0.22‰ at 300 K to 0.29 ± 0.14‰ at 600 K. Other theoretical studies also reported the same conclusion (Colla et al., 2018; Gao et al., 2018), but their calculations show much larger $10^3\ln\alpha_{brucite\text{-}Mg\_aq}$. In contrast, Li et al. (2014) found that the experimentally measured Mg isotope fractionation between brucite and solution ($\Delta^{26}Mg_{brucite\text{-}solution}$) increased from −0.3‰ at 280 K to 0‰ at 313 K, significantly deviating from our calculated results. The kinetic isotope effect was speculated to be responsible for the variation of $\Delta^{26}Mg_{brucite\text{-}solution}$ with temperature (Li et al., 2014). In addition, Wimpenny et al. (2014a,b) reported a $\Delta^{26}Mg_{brucite\text{-}solution}$ value of 0.5‰ at 323 K from the brucite growth experiments lasting 323 days. This long-term experiment may have approached isotope equilibrium and the measured $\Delta^{26}Mg_{brucite\text{-}solution}$ at equilibrium is consistent with our calculated results within the uncertainty (Fig. 5e). The small offset between experimental data and our result can be explained by the precipitation of magnesite in the solution (Wimpenny et al., 2014a,b), which will make the solution have heavier Mg isotope composition because the β factor of magnesite is lower than that of aqueous Mg^{2+} (Fig. 3). Consequently, the experimentally measured positive $\Delta^{26}Mg_{brucite\text{-}solution}$ will decrease to a smaller value when magnesite precipitates from the solution. Furthermore, lizardite, present as a major mineral in serpentine marbles, is also enriched in heavy Mg isotopes relative to the aqueous Mg^{2+}. The calculated $10^3\ln\alpha_{lizardite\text{-}Mg\_aq}$ changes from 4.70 ± 0.50‰ at 300 K to 1.20 ± 0.22‰ at 600 K (Fig. 5f). These data provide a guideline to understand Mg isotope fractionations during serpentinization.

5. CONCLUSIONS

Equilibrium Mg isotope fractionation among carbonates, brucite, lizardite, and aqueous Mg^{2+} were calculated based on the DFT. The FPMD simulations for aqueous Mg^{2+} indicate that the PRDF of Mg-O pair does not change with aqueous Mg concentration when Mg:H_2O is lower than 1:50. Thirty-five snapshots from the FPMD trajectories were extracted every 1000 steps after equilibration and the atomic positions of each snapshot were well relaxed. For minerals, their cell parameters as well as

atomic positions were both well relaxed, and the average Mg–O bond length increases in the order of lizardite < brucite ~ dolomite < magnesite < calcite < aragonite.

The β factors of minerals and aqueous Mg^{2+} were also obtained from the vibrational properties calculated based on the periodic boundary conditions. The β factor decreases in the sequence of lizardite > brucite > aqueous Mg^{2+} > dolomite > magnesite > calcite > aragonite. Our calculations within the GGA also confirm the Mg concentration effect on the β factor of calcite, and further show that the concentration effect is negligible when Mg/(Mg + Ca) is lower than a threshold value (i.e., 1/32 for calcite). The β factor is linearly correlated with the average force constant $\langle F \rangle$ of Mg, which is significantly affected by the average Mg-O bond length and the coordination number.

Our calculations reveal large equilibrium Mg isotope fractionations between minerals and aqueous Mg^{2+} ($10^3\ln\alpha_{minerals\text{-}Mg\_aq}$), consistent with experimentally measured Mg isotope fractionations between minerals (dolomite, magnesite, and brucite) and solution at equilibrium. Such agreements highlight the importance of the accurate description of FPMD simulations for aqueous Mg^{2+}. Compared to aqueous Mg^{2+}, carbonates are enriched in light Mg isotopes but brucite and lizardite show enrichment in heavy Mg isotopes. Among all minerals, $10^3\ln\alpha_{aragonite\text{-}Mg\_aq}$ is the largest, which is up to −14‰ at 300 K. $10^3\ln\alpha_{calcite\text{-}Mg\_aq}$ is not only controlled by temperature, but also significantly affected Mg content in calcite. Larger negative $10^3\ln\alpha_{calcite\text{-}Mg\_aq}$ occurs at lower Mg content in calcite. This study provides reliable estimates for equilibrium Mg isotope fractionation factors between minerals and aqueous Mg^{2+}, which are critical for the potential applications of Mg isotopes in geochemical processes.

ACKNOWLEDGMENTS

This study is financially supported by the Strategic Priority Research Program (B) of the Chinese Academy of Sciences (XDB18000000), the Natural Science Foundation of China (41473011, 41721002, 41325011), the Fundamental Research Funds for the Central Universities (WK2080000078), and Special Program for Applied Research on Super Computation of the NSFC-Guangdong Joint Fund. The computations were conducted partly in Supercomputing Center of the University of Science and Technology of China.

APPENDIX A. SUPPLEMENTARY MATERIAL

Supplementary data to this article can be found online at https://doi.org/10.1016/j.gca.2019.01.042.

REFERENCES

Anbar A. D. and Rouxel O. (2007) Metal stable isotopes in paleoceanography. *Annu. Rev. Earth Planet. Sci.* **35**, 717–746.

Beinlich A., Mavromatis V., Austrheim H. and Oelkers E. H. (2014) Inter-mineral Mg isotope fractionation during hydrothermal ultramafic rock alteration – Implications for the global Mg-cycle. *Earth Planet. Sci. Lett.* **392**, 166–176.

Bigeleisen J. and Mayer M. G. (1947) Calculation of equilibrium constants for isotopic exchange reactions. *J. Chem. Phys.* **15**, 261.

Blöchl P. E. (1994) Projector augmented-wave method. *Phys. Rev. B* **50**, 17953–17979.

Colla C. A., Casey W. H. and Ohlin C. A. (2018) Computational prediction of Mg-isotope fractionation between aqueous $[Mg(OH_2)_6]^{2+}$ and brucite. *Geochim. Cosmochim. Acta* **227**, 64–74.

Dauphas N., Roskosz M., Alp E. E., Golden D. C., Sio C. K., Tissot F. L. H., Hu M. Y., Zhao J., Gao L. and Morris R. V. (2012) A general moment NRIXS approach to the determination of equilibrium Fe isotopic fractionation factors: Application to goethite and jarosite. *Geochim. Cosmochim. Acta* **94**, 254–275.

Ducher M., Blanchard M. and Balan E. (2018) Equilibrium isotopic fractionation between aqueous Zn and minerals from first-principles calculations. *Chem. Geol.* **483**, 342–350.

Dupuis R., Benoit M., Nardin E. and Méheut M. (2015) Fractionation of silicon isotopes in liquids: The importance of configurational disorder. *Chem. Geol.* **396**, 239–254.

Fantle M. S. and Higgins J. (2014) The effects of diagenesis and dolomitization on Ca and Mg isotopes in marine platform carbonates: Implications for the geochemical cycles of Ca and Mg. *Geochim. Cosmochim. Acta* **142**, 458–481.

Feng C., Qin T., Huang S., Wu Z. and Huang F. (2014) First-principles investigations of equilibrium calcium isotope fractionation between clinopyroxene and Ca-doped orthopyroxene. *Geochim. Cosmochim. Acta* **143**, 132–142.

Gao C., Cao X., Liu Q., Yang Y., Zhang S., He Y., Tang M. and Liu Y. (2018) Theoretical calculation of equilibrium Mg isotope fractionations between minerals and aqueous solutions. *Chem. Geol.* **488**, 62–75.

Giuffre A. J., Gagnon A. C., De Yoreo J. J. and Dove P. M. (2015) Isotopic tracer evidence for the amorphous calcium carbonate to calcite transformation by dissolution–reprecipitation. *Geochim. Cosmochim. Acta* **165**, 407–417.

Higgins J. A. and Schrag D. P. (2010) Constraining magnesium cycling in marine sediments using magnesium isotopes. *Geochim. Cosmochim. Acta* **74**, 5039–5053.

Higgins J. A. and Schrag D. P. (2015) The Mg isotopic composition of Cenozoic seawater – evidence for a link between Mg-clays, seawater Mg/Ca, and climate. *Earth Planet. Sci. Lett.* **416**, 73–81.

Hill P. S. and Schauble E. A. (2008) Modeling the effects of bond environment on equilibrium iron isotope fractionation in ferric aquo-chloro complexes. *Geochim. Cosmochim. Acta* **72**, 1939–1958.

Huang K.-J., Teng F.-Z., Wei G.-J., Ma J.-L. and Bao Z.-Y. (2012) Adsorption- and desorption-controlled magnesium isotope fractionation during extreme weathering of basalt in Hainan Island, China. *Earth Planet. Sci. Lett.* **359–360**, 73–83.

Huang F., Chen L., Wu Z. and Wang W. (2013) First-principles calculations of equilibrium Mg isotope fractionations between garnet, clinopyroxene, orthopyroxene, and olivine: Implications for Mg isotope thermometry. *Earth Planet. Sci. Lett.* **367**, 61–70.

Huang F., Wu Z., Huang S. and Wu F. (2014) First-principles calculations of equilibrium silicon isotope fractionation among mantle minerals. *Geochim. Cosmochim. Acta* **140**, 509–520.

Huang J., Li S.-G., Xiao Y., Ke S., Li W.-Y. and Tian Y. (2015) Origin of low $\delta^{26}Mg$ Cenozoic basalts from South China Block and their geodynamic implications. *Geochim. Cosmochim. Acta* **164**, 298–317.

Husson J. M., Higgins J. A., Maloof A. C. and Schoene B. (2015) Ca and Mg isotope constraints on the origin of Earth's deepest $\delta^{13}C$ excursion. *Geochim. Cosmochim. Acta* **160**, 243–266.

Immenhauser A., Buhl D., Richter D., Niedermayr A., Riechelmann D., Dietzel M. and Schulte U. (2010) Magnesium-isotope fractionation during low-Mg calcite precipitation in a limestone cave – Field study and experiments. *Geochim. Cosmochim. Acta* **74**, 4346–4364.

Kasemann S. A., Pogge von Strandmann P. A. E., Prave A. R., Fallick A. E., Elliott T. and Hoffmann K.-H. (2014) Continental weathering following a Cryogenian glaciation: Evidence from calcium and magnesium isotopes. *Earth Planet. Sci. Lett.* **396**, 66–77.

Kowalski P. M. and Jahn S. (2011) Prediction of equilibrium Li isotope fractionation between minerals and aqueous solutions at high P and T: An efficient ab initio approach. *Geochim. Cosmochim. Acta* **75**, 6112–6123.

Li W., Chakraborty S., Beard B. L., Romanek C. S. and Johnson C. M. (2012) Magnesium isotope fractionation during precipitation of inorganic calcite under laboratory conditions. *Earth Planet. Sci. Lett.* **333–334**, 304–316.

Li W., Beard B. L., Li C. and Johnson C. M. (2014) Magnesium isotope fractionation between brucite [$Mg(OH)_2$] and Mg aqueous species: Implications for silicate weathering and biogeochemical processes. *Earth Planet. Sci. Lett.* **394**, 82–93.

Li W., Beard B. L., Li C., Xu H. and Johnson C. M. (2015) Experimental calibration of Mg isotope fractionation between dolomite and aqueous solution and its geological implications. *Geochim. Cosmochim. Acta* **157**, 164–181.

Li S.-G., Yang W., Ke S., Meng X., Tian H., Xu L., He Y., Huang J., Wang X.-C., Xia Q., Sun W., Yang X., Ren Z.-Y., Wei H., Liu Y., Meng F. and Yan J. (2016) Deep carbon cycles constrained by a large-scale mantle Mg isotope anomaly in eastern, China. *Natl. Sci. Rev.* **4**, nww070.

Liu D., Zhao Z., Zhu D.-C., Niu Y., Widom E., Teng F.-Z., DePaolo D. J., Ke S., Xu J.-F., Wang Q. and Mo X. (2015) Identifying mantle carbonatite metasomatism through Os–Sr–Mg isotopes in Tibetan ultrapotassic rocks. *Earth Planet. Sci. Lett.* **430**, 458–469.

Liu X., Qi Y., Zheng D., Zhou C., He L. and Huang F. (2018) Diffusion coefficients of Mg isotopes in $MgSiO_3$ and Mg_2SiO_4 melts calculated by first-principles molecular dynamics simulations. *Geochim. Cosmochim. Acta* **223**, 364–376.

Mavromatis V., Gautier Q., Bosc O. and Schott J. (2013) Kinetics of Mg partition and Mg stable isotope fractionation during its incorporation in calcite. *Geochim. Cosmochim. Acta* **114**, 188–203.

Mavromatis V., Purgstaller B., Dietzel M., Buhl D., Immenhauser A. and Schott J. (2017) Impact of amorphous precursor phases on magnesium isotope signatures of Mg-calcite. *Earth Planet. Sci. Lett.* **464**, 227–236.

Méheut M., Lazzeri M., Balan E. and Mauri F. (2009) Structural control over equilibrium silicon and oxygen isotopic fractionation: A first-principles density-functional theory study. *Chem. Geol.* **258**, 28–37.

Ohtaki H. and Radnai T. (1993) Structure and dynamics of hydrated ions. *Chem. Rev.* **93**, 1157–1204.

Pearce C. R., Saldi G. D., Schott J. and Oelkers E. H. (2012) Isotopic fractionation during congruent dissolution, precipitation and at equilibrium: Evidence from Mg isotopes. *Geochim. Cosmochim. Acta* **92**, 170–183.

Perdew J. P., Burke K. and Ernzerhof M. (1996) Generalized gradient approximation made simple. *Phys. Rev. Lett.* **77**, 3865–3868.

Pinilla C., Blanchard M., Balan E., Natarajan S. K., Vuilleumier R. and Mauri F. (2015) Equilibrium magnesium isotope fractionation between aqueous Mg^{2+} and carbonate minerals: Insights from path integral molecular dynamics. *Geochim. Cosmochim. Acta* **163**, 126–139.

Pogge von Strandmann P. A. E., Burton K. W., James R. H., van Calsteren P., Gislason S. R. and Sigfússon B. (2008) The influence of weathering processes on riverine magnesium isotopes in a basaltic terrain. *Earth Planet. Sci. Lett.* **276**, 187–197.

Pokrovsky B. G., Mavromatis V. and Pokrovsky O. S. (2011) Co-variation of Mg and C isotopes in late Precambrian carbonates of the Siberian Platform: A new tool for tracing the change in weathering regime? *Chem. Geol.* **290**, 67–74.

Purgstaller B., Mavromatis V., Immenhauser A. and Dietzel M. (2016) Transformation of Mg-bearing amorphous calcium carbonate to Mg-calcite – In situ monitoring. *Geochim. Cosmochim. Acta* **174**, 180–195.

Qin T., Wu F., Wu Z. and Huang F. (2016) First-principles calculations of equilibrium fractionation of O and Si isotopes in quartz, albite, anorthite, and zircon. *Contrib. Mineral. Petrol.* **171**, 91.

Richet P., Bottinga Y. and Javoy M. (1977) A review of hydrogen, carbon, nitrogen, oxygen, sulphur, and chlorine stable isotope fractionation among gaseous molecules. *Annu. Rev. Earth Planet. Sci.* **5**, 65–110.

Ruiz-Hernandez S. E., Grau-Crespo R., Almora-Barrios N., Wolthers M., Ruiz-Salvador A. R., Fernandez N. and De Leeuw N. H. (2012) Mg/Ca partitioning between aqueous solution and aragonite mineral: A molecular dynamics study. *Chem. - A Eur. J.* **18**, 9828–9833.

Rustad J. R., Casey W. H., Yin Q.-Z., Bylaska E. J., Felmy A. R., Bogatko S. A., Jackson V. E. and Dixon D. A. (2010) Isotopic fractionation of Mg^{2+}(aq), Ca^{2+}(aq), and Fe^{2+}(aq) with carbonate minerals. *Geochim. Cosmochim. Acta* **74**, 6301–6323.

Saenger C. and Wang Z. (2014) Magnesium isotope fractionation in biogenic and abiogenic carbonates: Implications for paleoenvironmental proxies. *Quat. Sci. Rev.* **90**, 1–21.

Saulnier S., Rollion-Bard C., Vigier N. and Chaussidon M. (2012) Mg isotope fractionation during calcite precipitation: An experimental study. *Geochim. Cosmochim. Acta* **91**, 75–91.

Schauble E. A. (2011) First-principles estimates of equilibrium magnesium isotope fractionation in silicate, oxide, carbonate and hexaaquamagnesium (2+) crystals. *Geochim. Cosmochim. Acta* **75**, 844–869.

Schauble E., Rossman G. R. and Taylor H. P. (2004) Theoretical estimates of equilibrium chromium-isotope fractionations. *Chem. Geol.* **205**, 99–114.

Schott J., Mavromatis V., Fujii T., Pearce C. R. and Oelkers E. H. (2016) The control of carbonate mineral Mg isotope composition by aqueous speciation: Theoretical and experimental modeling. *Chem. Geol.* **445**, 120–134.

Teng F.-Z. (2017) Magnesium isotope geochemistry. *Rev. Miner. Geochem.* **82**, 219–287.

Teng F.-Z., Li W.-Y., Rudnick R. L. and Gardner L. R. (2010) Contrasting lithium and magnesium isotope fractionation during continental weathering. *Earth Planet. Sci. Lett.* **300**, 63–71.

Tipper E. T., Galy A., Gaillardet J., Bickle M. J., Elderfield H. and Carder E. A. (2006) The magnesium isotope budget of the modern ocean: Constraints from riverine magnesium isotope ratios. *Earth Planet. Sci. Lett.* **250**, 241–253.

Togo A. and Tanaka I. (2015) First principles phonon calculations in materials science. *Scr. Mater.* **108**, 1–5.

Urey H. C. (1947) The thermodynamic properties of isotopic substances ed. S.-I. Karato. *J. Chem. Soc.* **562**.

Wang Z., Hu P., Gaetani G., Liu C., Saenger C., Cohen A. and Hart S. (2013) Experimental calibration of Mg isotope fractionation between aragonite and seawater. *Geochim. Cosmochim. Acta* **102**, 113–123.

Wang W., Qin T., Zhou C., Huang S., Wu Z. and Huang F. (2017a) Concentration effect on equilibrium fractionation of Mg-Ca isotopes in carbonate minerals: Insights from first-principles calculations. *Geochim. Cosmochim. Acta* **208**, 185–197.

Wang W., Zhou C., Qin T., Kang J., Huang S., Wu Z. and Huang F. (2017b) Effect of Ca content on equilibrium Ca isotope fractionation between orthopyroxene and clinopyroxene. *Geochim. Cosmochim. Acta* **219**, 44–56.

Wang W. and Wu Z. (2018) Elasticity of corundum at high pressures and temperatures: implications for pyrope decomposition and Al-content effect on elastic properties of bridgmanite. *J. Geophys. Res. Solid Earth* **123**, 1201–1216.

Wentzcovitch R. M., Yu Y. G. and Wu Z. (2010) Thermodynamic properties and phase relations in mantle minerals investigated by first principles quasiharmonic theory. *Rev. Mineral. Geochem.* **71**, 59–98.

Wimpenny J., Colla C. A., Yin Q. Z., Rustad J. R. and Casey W. H. (2014a) Investigating the behaviour of Mg isotopes during the formation of clay minerals. *Geochim. Cosmochim. Acta* **128**, 178–194.

Wimpenny J., Yin Q.-Z., Tollstrup D., Xie L.-W. and Sun J. (2014b) Using Mg isotope ratios to trace Cenozoic weathering changes: A case study from the Chinese Loess Plateau. *Chem. Geol.* **376**, 31–43.

Wu Z., Huang F. and Huang S. (2015) Isotope fractionation induced by phase transformation: First-principles investigation for Mg_2SiO_4. *Earth Planet. Sci. Lett.* **409**, 339–347.

Yang W., Teng F.-Z., Zhang H.-F. and Li S.-G. (2012) Magnesium isotopic systematics of continental basalts from the North China craton: Implications for tracing subducted carbonate in the mantle. *Chem. Geol.* **328**, 185–194.

Young E. D., Tonui E., Manning C. E., Schauble E. and Macris C. A. (2009) Spinel–olivine magnesium isotope thermometry in the mantle and implications for the Mg isotopic composition of Earth. *Earth Planet. Sci. Lett.* **288**, 524–533.

Associate editor: Wolfgang Bach